Failure Analysis of Bolted Joints in Cross-ply Composite Laminates Using Cohesive Zone Elements

A. Ataş[1], C. Soutis[2]

Abstract: A strength prediction method is presented for double-lap single fastener bolted joints of cross-ply carbon fibre reinforced plastic (CFRP) composite laminates using cohesive zone elements (CZEs). Three-dimensional finite element models were developed and CZEs were inserted into subcritical damage planes identified from X-ray radiographs. The method makes a compromise between the experimental correlation factors (dependant on lay-up, stacking sequence and joint geometry) and three material properties (fracture energy, interlaminar strength and nonlinear shear stress-strain response). Strength of the joints was determined from the predicted load-displacement curves considering sub-laminate and ply-level scaling effects. The predictions are in a reasonable agreement with the experimental data.

Keywords: Composite laminates, bolted joints, strength prediction, finite elements method (FEM), subcritical damage modelling, cohesive zone elements (CZEs).

1 Introduction

Strength prediction of a mechanical joint is the determination of the maximum load or displacement which the joint could sustain before its final failure. However, there is no consensus among engineers on the definition of the final failure. The first non-linearity, the first or the global peak point (maximum load sustained by the joint) in the load-displacement curve and the amount of hole deformation have been generally used to define experimental failure load (Collings 1982, Wang et al. 1996, Dano et al. 2000, McCarthy et al. 2002, Chang and Qing 2003, Atas et al. 2009, Sen and Sayman 2009).

On the other hand, analytical and FE stress predictions along the fastener hole

---

[1] Department of Mechanical Engineering, Balıkesir Üniversitesi, Çağış Kampüsü 10145, Balıkesir, Turkey.

[2] School of Mechanical, Aerospace & Civil Engineering, University of Manchester, Manchester, M13 9PL, UK.

boundary have been used to define the failure load based on various theories such as maximum stress/strain criteria (Waszczak and Cruse 1971, Crews and Naik 1986, Smith et al. 1987). These criteria can be applied to a layer of the laminate or to the whole laminate depending upon the methodology used. Although simple, these methods lead to underestimation of the joint strength because of omitting the stress redistribution due to the local subcritical damage mechanisms, e.g. matrix cracks, axial splits and delaminations.

Accordingly, methods were developed to account for subcritical damage mechanisms caused by the local high stress concentrations (Whitney and Nuismer 1974, Chang et al. 1982, Chang et al. 1984, Whitworth et al. 2008). Stresses were calculated at a so-called characteristic distance to determine the failure load in some models where only two experimentally defined parameters required: the characteristic distance and the unnotched laminate strength. They have been widely used owing to their simplicity, although the need to determine the unnotched strength and characteristic distance of each different laminate system are the drawbacks of these methods. Other methods were also developed to take into account the subcritical damage mechanisms based on the relation between elastic isotropic stress concentration factors and the stress concentration factors at failure of the specific material system of the same joint geometry (Hart-Smith 2003, Hart-Smith 2004).

Progressive failure analysis (PFA) is a methodology which simulates the initiation and growth of the damage in mechanical joints based on stress analysis, implementing failure criteria and material property degradation rules (Camanho and Matthews 1999, Dano et al. 2000, Tserpes et al. 2001, Icten and Karakuzu 2002, Chang and Qing 2003, McCarthy et al. 2005, Xiao and Ishikawa 2005, Atas et al. 2010, Atas et al. 2012, Wang et al. 2012). The effect of the subcritical damage on the global response was simulated by reducing the material properties of the failed elements. Special attention must be paid to the material degradation rules which are key parameters representing the subcritical damage. Generally, a parametric study is necessary to determine the individual degradation factors for the best fit to experimental data of a certain laminate configuration. Then, the same factors can be used to predict the joint strengths of various joint geometries and laminate configurations of the same material system with varied success.

Fracture mechanics based damage zone modelling (DZM) has been used to predict the strength of the composite joints as an alternative to the characteristic distance and the PFA methods (Hollmann 1996). The DZM can be thought as a PFA methodology since the initiation and the growth of damage are taken into consideration. This method requires the laminate strength and fracture energy properties to be determined experimentally for each laminate type as input parameters. Although providing good predictions, this method has limited use compared with the

PFA methodology.

Based on the literature review of state-of-the-art techniques, it is clear that widely used strength prediction methods for bolted joints in composite laminates rely on some form of experimental correlation factors. These correlation factors are functions of the material system, joint geometry, clamping torque, laminate lay-up and stacking sequence. The empirical dependency of the strength prediction methods thus limits their potential to specific design cases.

The aim of the present study was to develop a physics-based strength prediction method which is not referring to correlation factors used to account for the subcritical damage modes in the form of resin cracking and delamination. Explicit modelling of these subcritical damage modes is suggested in order to render the use of the correlation factors redundant with a compromise of fracture energy, interlaminar strength and nonlinear matrix shear stress-strain response inputs to the FE analysis. X-ray radiography was used in order to identify the subcritical damage locations and three-dimensional (3-D) FE models were created with the explicit definition of the damage modes. Cohesive zone elements (CZEs) were inserted in selected regions in order to simulate the subcritical damage initiation and growth, as will be detailed in the following sections.

2   Materials and testing methods

The material system used in this study is HTS40/977-2 carbon fibre-epoxy in the form of pre-impregnated (prepreg) tape. The prepreg tapes were made of unidirectional high tensile strength/standard modulus aerospace grade carbon fibres (Toho Tenax®, HTS40-F13-12K-800tex) pre-impregnated with $177°C$ curing toughened epoxy resin (Cycom®977-2). The nominal thickness of the prepreg tape is 0.25mm with an approximate fibre volume fraction of 58% (Jumahat et al. 2010). The composite laminates were fabricated by the hand lay-up technique in an autoclave according to the manufacturer's recommended curing procedure. Typical specimen geometry is shown in Fig. 1 with definitions of the width (w), free edge distance (e), hole diameter (d) and thickness (t). The x-yand1-2 coordinate systems define the global laminate and local material coordinate systems, respectively. The angle ϕ defines the layer orientation angle with respect to the x (loading) axis and angle θ define the circumferential co-ordinate direction around the hole boundary.

A diamond tip saw was used to cut the laminates to dimensions with special care given to the precise alignment of the laminates. Fastener holes of 6mm were drilled with a backing plate in order to prevent drilling induced splitting and delamination failure, something difficult to avoid especially in very thin laminates. The composite plates were inspected by X-ray radiography to establish specimen quality.
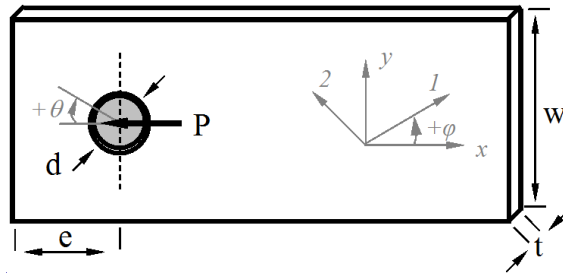
Figure 1: Geometrical definitions of a bolt-loaded composite laminate

Double-lap single-bolted shear loading fixtures were manufactured in accordance with the ASTM standard D5961/D5961 (ASTM 2001). 12.9 grade steel bolts of 5.95mm in diameter were used to load the specimens with a clearance of 0.05mm. Tests were conducted at room temperature with a Hounsfield electromechanical testing machine, at a 1mm/min loading rate. Applied load and the cross-head displacement were recorded by a computer aided data acquisition system. Tests were stopped after a significant (approximately 30 %) load drop was observed in the load-displacement curve, according to ASTM standard (ASTM 2001). Finger-tightened joints were chosen according to standard design practices where the fully-tightened joints are assumed to be loosened due to service loading conditions. After testing, specimens were inspected using penetrant enhanced X-ray radiography (Soutis et al. 1991).

Cross-ply specimens are often not used in practical structural applications. However, they were used in this work due to their relatively apparent damage locations to facilitate comparison with the FE predictions and test theoretical damage models and assumptions. $[90°/0°]_s$, sublaminate-level scaled $[90°/0°]_{2s}$ and ply-level scaled $[90_2°/0_2°]_s$ laminates were tested considering the scaling effects on the strength of bolted joints (Soutis and Lee 2008). Laminates with 90° outer layers were used to provide the same degree of constraint for the inner 0° layers (Kortschot and Beaumont 1990). The width-to-hole diameter and edge distance-to-hole diameter ratios were kept constant for d=6mm hole diameter (w/d=6 and e/d=3).

3   Experimental observations

An X-ray radiograph of a finger-tight bolted joint in the $[90°/0°]_s$ lay-up is shown in Fig. 2, where transverse matrix cracks, axial splitting, compressive fibre failure and delamination damage can be observed.

The characteristic "V" shape of the fibre compressive failure observed in almost
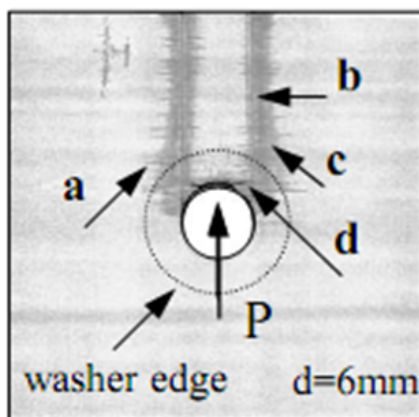
Figure 2: An X-ray radiograph showing damage in a finger-tight bolted $[90°/0°]_s$ lay-up at failure: a) transverse matrix cracks, b) axial splitting, c) delamination, d) compressive fibre failure in 0° layers

all cross-ply lay-ups by X-ray radiography is similar to that of 0° laminates (transversely constrained from splitting) reported by Collings (Collings 1982) as shown in Fig. 3(i). This is a fibre instability failure mode, observed also in open hole specimens loaded in compression as shown in Fig 3(ii), that initiates due to local fibre buckling and propagates across the specimen width, forming a kink band zone (fibre kinking) (Soutis and Fleck 1990, Soutis 1991, Jumahat et al. 2010).

Figure 4 shows a schematic of the subcritical in-plane damage locations observed from the X-ray radiographs of the cross-ply lay-ups. The extent of the transverse matrix cracks dispersed along the axial splits as shown in X-ray radiographs. However, it has been shown that those transverse matrix cracks can be represented as a single crack where the maximum stress concentration occurs for the centre notched specimens without affecting the subcritical damage predictions significantly (Wisnom and Chang 2000), which of course is an approximation. Thus, based on this assumption, the transverse matrix cracks were represented as single cracks at the maximum stress concentration locations ($\theta = \pm 90°$) in order to reduce the modelling efforts and the computational time. Axial split planes within the 0° layers were extended from the hole edge at $\theta = \pm 90°$ to the free edge as observed from the radiographs and depicted schematically in Fig. 4.

The compressive fibre failure occurs around 90-95% of the failure load and merges with the axial splits which were modelled discretely. Although additional work
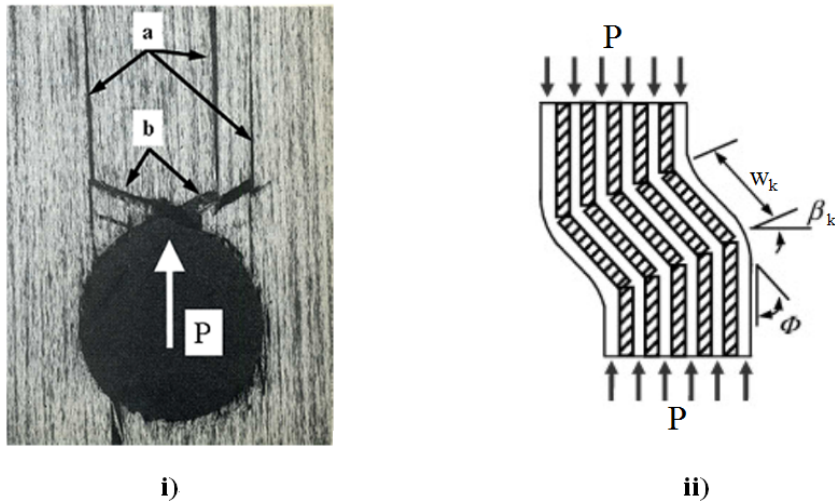
Figure 3: (i) a) axial splitting, b) compressive fibre failure in a laterally constrained [0°] laminate (hole diameter is 6.35mm) (Collings 1982), **(ii)** formation of kink band zone (w_k: kink band width, β_k: boundary orientation and Φ: inclination angle) (Jumahat et al. 2010)

is required in order to show the influence of the compressive fibre failure on the global failure load, it was omitted in the FE models as it would cause a considerable amount of modelling and computational effort.
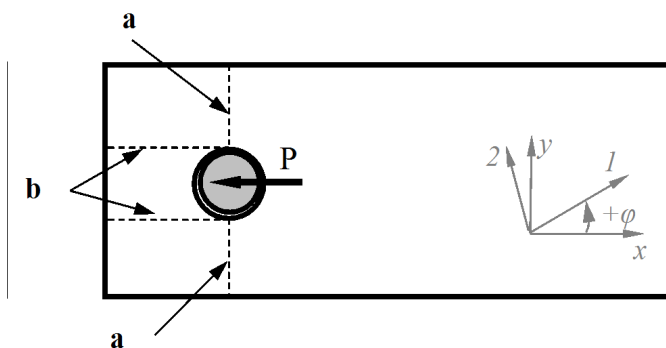

Figure 4: Subcritical in-plane damage locations observed in cross-ply lay-ups: a) transverse matrix cracking planes in 90° layers, b) axial split planes in 0° layers

4 Finite element modelling

Figure 5 shows the 3-D finite element model developed for the $[90°/0°]_s$ layup using the ANSYS software (2009) based on the subcritical damage planes depicted in Fig. 4 and delamination planes between the adjacent layers. Other two layups have the same in-plane dimensions. One element per laminate layer approach used to model each of the 0.25mm thick layers using SOLID185 linear 8-noded brick elements. The advantage of the geometrical symmetry of the model with respect to *xy* plane was used to reduce the computational time (symmetry conditions also applicable with respect to *xz* plane for the cross-ply layups). All degrees of freedom were constrained at the fixed end of the laminate in order to simulate the fully clamped laminate end. An incremental displacement was applied to the bolt along the (negative) x-direction in order to load the specimen.

The bolt and the washer were modelled as steel deformable bodies using SOLID185 linear 8-noded brick elements. The steel material properties were E = 210 GPa and $v = 0.3$. Contact algorithms were defined between the bolt shank and the laminate hole boundary and between the washer and the top surface of the laminate using CONTA174 and TARGE170 elements. The clearance between the bolt and the laminate was set to an experimentally measured value of 0.05mm. The coefficient of friction was assumed to be 0.2 in all contact surfaces (Ireman 1998). An augmented Lagrangian contact algorithm was used to check the amount of penetration against the allowable tolerance.
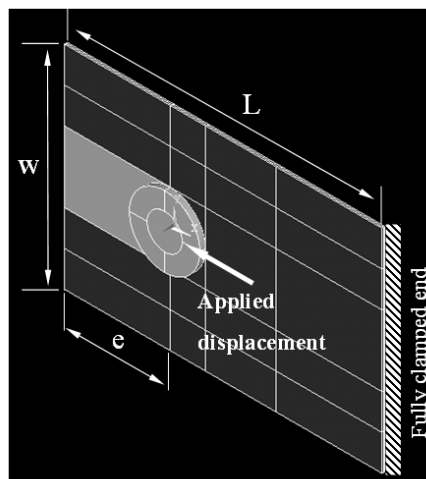

Figure 5: Finite element model for the $[90°/0°]_s$ layup (*L*, *W* and *e* stand for the length, width and edge distance of the model, respectively. *L*=54mm)

Elastic material properties, strengths and interfacial properties of the HTS40/977-2 are given in Tables 1 to 3. The interfacial properties were adopted from T300/977-2 CFRP material system owing to the same toughened epoxy matrix material used for both pre-pregs. Together with the high strength fibres of similar characteristics (HTS40 and T300), both material systems also exhibit very close elastic material properties (Goyal et al. 2004). The interfacial properties, Table 3, were used to model both the axial splits (within the 0° layers) and delamination subcritical damage modes through the CZEs (2009).

Table 1: Elastic properties of HTS40/977-2 (Heimbs et al. 2009)

E_{11}(MPa)	$E_{22}=E_{33}$(MPa)	$G_{12}=G_{13}$(MPa)	G_{23}(MPa)	$v_{12=}v_{13}$	v_{23}
153000	10300	5200	3430	0.3	0.5

Table 2: Strengths of HTS40/977-2 (Heimbs et al. 2009)

X_T(MPa)	X_C(MPa)	$Y_T=Z_T$(MPa)	$Y_C=Z_C$(MPa)	$S_{XY}=S_{XZ}=S_{YZ}$(MPa)
2540	1500	82	236	90

Table 3: Interfacial properties used for HTS40/977-2 adopted from T300/977-2 (Goyal et al. 2004, Harper and Hallett 2008)

G_{IC} (N/mm)	G_{IIC} (N/mm)	σ_{max} (MPa)	τ_{max} (MPa)	K_n (N/mm^3)	K_t(N/mm^3)
0.352	1.45	60	80	1x10^5	1x10^5

It has been shown that the inclusion of nonlinear in-plane shear stress-strain behaviour has an important influence, especially on the strength predictions of cross-ply bolted specimens (Dano et al. 2000, Shokrieh and Lessard 1996). A subroutine was developed using the following function in order to model the nonlinear shear stress-strain behaviour (Dano et al. 2000, Shokrieh and Lessard 1996, Hahn and Tsai 1973):

$$\gamma_{12} = \left(\frac{1}{G_{12}^0} \right) \tau_{12} + \alpha_{nl}\, \tau_{12}^3 \tag{1}$$

Equation 1 arranged to give a linear function in order to be implemented into the FE software, as follows:

$$\tau_{12}^{(i+1)} = G_{12}\gamma_{12}^{(i+1)} = (1-d_{nl})\, G_{12}^0 \gamma_{12}^{(i+1)} \tag{2}$$

where G^0_{12}, τ_{12}, γ_{12}, and i are the initial shear modulus, shear stress, shear strain, increment number, respectively. d_{nl} is the damage factor expressed in Eq. (3) and α_{nl} is a parameter which is determined experimentally.

$$d_{nl} = \frac{3\,\alpha_{nl}\,G^0_{12}\left(\tau^{(i)}_{12}\right)^2 - 2\,\alpha_{nl}\left(\tau^{(i)}_{12}\right)^3 / \gamma^{(i)}_{12}}{1 + 3\,\alpha_{nl}\,G^0_{12}\left(\tau^{(i)}_{12}\right)^2} \tag{3}$$

The nonlinear in-plane shear stress-strain response of the HTS40/977-2 composite system was investigated (Jumahat et al. 2010). Figure 6 (a) shows the experimentally determined and analytical (Eq. 4) nonlinear shear stress-strain curves of the $[\pm45]_{2s}$ laminate under tensile loading, Fig. 6 (b).
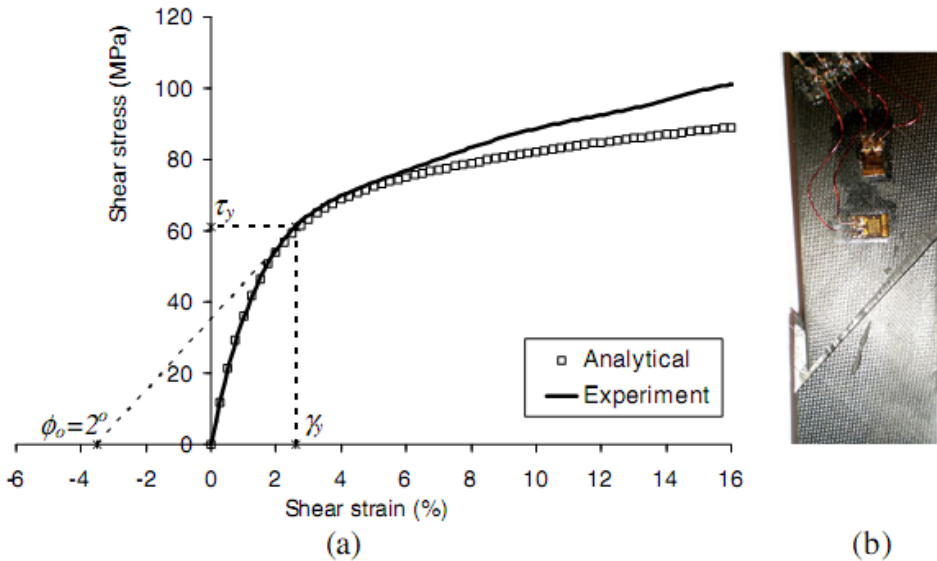

Figure 6: (a) In-plane shear stress-strain response of a $[\pm45]_{2s}$ HTS40/977-2 laminate and (b) a failed specimen (Jumahat et al. 2010)

$$\tau(\gamma) = \tau_y\left[1 - \exp\left(-\frac{G^e_{12}\gamma}{\tau_y}\right)\right] + (\tau_{ult} - \tau_y)\left[1 - \exp\left(-\frac{G^p_{12}\gamma}{\tau_{ult} - \tau_y}\right)\right] \tag{4}$$

where τ_y, τ_{ult}, G^e_{12}, G^p_{12} are the shear yield stress, in-plane shear strength, elastic shear modulus and the plastic shear modulus, respectively.

It is clear from Fig. 6 that Equation 4 closely represents the nonlinear behaviour of the HTS40/977-2 material system. For the present study α_{nl} is obtained as 8×10^{-8} MPa^{-3} from the best fit of the Equations 1 and 4 and implemented in the subroutine developed (Atas 2012).

Figures 7 (a) and (b) show the volume discretization and the mesh structure of 0° layers, respectively. Fully-integrated elements were used in the region where the subcritical damage modes were observed, depicted by the lighter zone in Fig. 7 (a), and reduced integration elements were used in other parts.
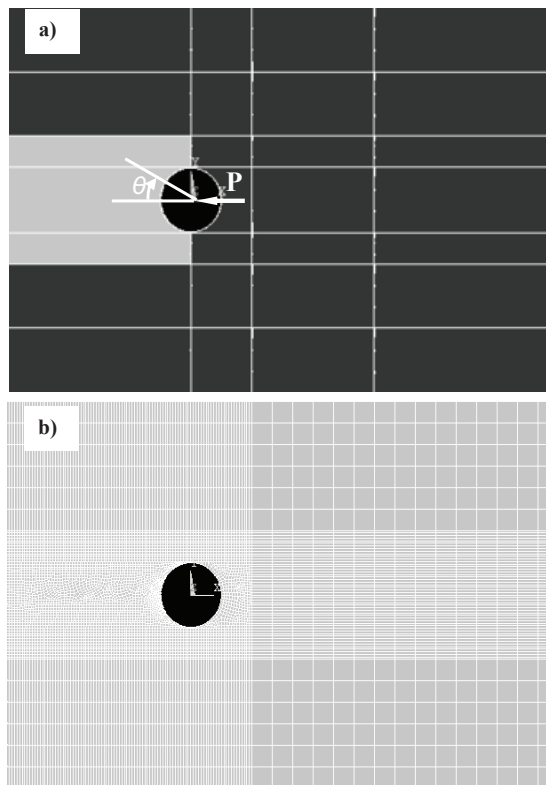
Figure 7: (a) FE volume discretization and (b) mesh structure of 0° layers

The axial splits in the 0° layers, observed from the X-ray radiographs, were extended from the hole edge towards the free edge of the laminates as shown in Fig. 8 (close-up views of Fig. 7). The split planes were modelled tangentially to the hole boundary, at a distance of one element thickness (0.25mm), as depicted by dashed lines in Fig. 8 (a). The reason for this was to avoid irregular element shapes

at the intersection of the hole edge and the tangent line.

Figure 9 shows the modelling details around the hole boundary marked with the white rectangle in Fig. 8 (a). Duplicate areas were used at the hole edge in order to allow the movement of the shear strip ahead of the fastener following the failure of the CZEs, whereas merged nodes ensured continuity between the volumes.
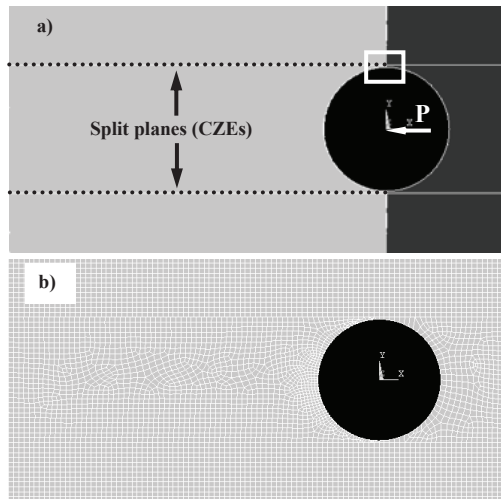

Figure 8: (a) Close-up view of the FE volume discretization and (b) mesh structure of 0˚ layers around the hole boundary.
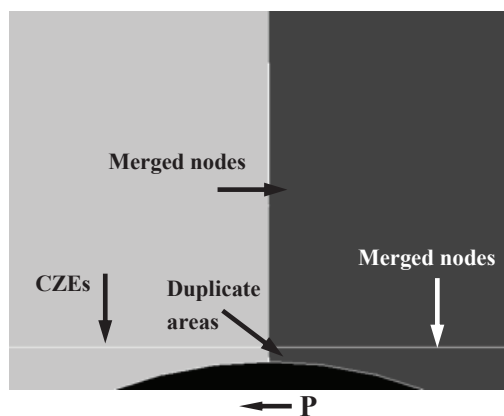

Figure 9: Modelling details around the hole boundary marked with the white rectangle in Fig. 8 (a).

Figure 10 shows the FE volume discretization, general and close-up mesh structure of 90° layers. Duplicate areas without any CZEs defined in between were created along the white vertical dashed lines in Fig. 10 (a) in order to model the transverse cracks. Transverse cracks occur at early stages of the loading process and it was assumed that they were fully developed at the beginning of the analyses due to the weak matrix dominated transverse strength of the 90° layers (Wisnom and Chang 2000).

Due to these duplicate areas, the 90° layer would not resist any loading if the layer alone were to be loaded by a frictionless pin. However, when located in a multi-directional laminate, part of the total load of the joint is transferred to the 90° layers by adjacent layers through shear stresses at the interfaces. In this manner, 90° layers contribute to the load carrying capability of the joints.

Since no contact constraints were defined between the duplicate areas, slight penetration occurred with increased loading between the adjacent volumes that the duplicate areas were connected to. Nevertheless, initial comparative analyses, including standard contact algorithms defined between the duplicate areas, showed that the stress field and the subcritical damage predictions were not affected due to this slight penetration. Consequently, no contact constraints were defined between those duplicate areas for the sake of increased computational efficiency.

The mesh density around the hole boundary and at the subcritical damage planes was determined according to equations (5) and (6) with the aim of having minimum of three elements within the cohesive zone length (l_{cz}). Mode I and Mode II cohesive zone lengths were calculated to be $l_{cz,I}$= 0.886mm and $l_{cz,II}$= 2.05mm, with M = 0.88 and E = 10.3 GPa. The value of the modulus of elasticity, E, in equations (5) and (6) is assumed to be equal to the transverse modulus E_{22} for orthotropic materials with transverse isotropy and M is a parameter (Atas 2012). Although the subcritical damage modes were shear dominated, $l_{cz,I}$ was used to determine the minimum element dimensions as suggested (Harper and Hallett 2008) and the in-plane dimensions of the elements in the critical locations were set to 0.25mm. This also satisfies the requirement of having an aspect ratio of 1.0 which ensures accurate calculation of interlaminar stresses (Atas et al. 2010). The mesh density was reduced away from those critical regions for the sake of computational efficiency.

$$l_{cz,I} = ME\frac{G_{IC}}{(\sigma_{max})^2} \tag{5}$$

$$l_{cz,II} = ME\frac{G_{IIC}}{(\tau_{max})^2} \tag{6}$$

The in-plane subcritical damage planes have been the focus thus far. Additionally, delamination damage planes were defined between all adjacent layers throughout
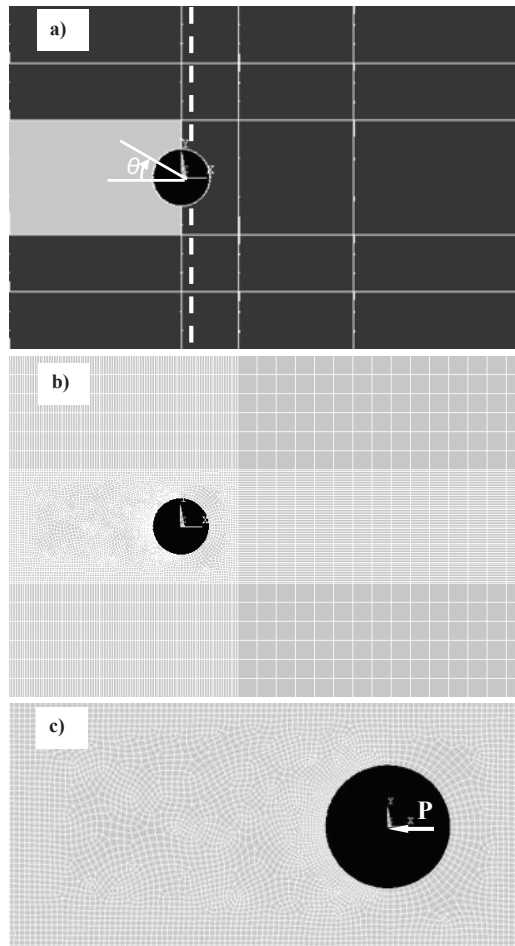
Figure 10: (a) FE volume discretization, (b) mesh structure and (c) close-up view of the mesh structure of 90˚ layers.

the whole interfaces. It is noted that each individual layer has a specific mesh structure which does not conform to the adjacent layers. The use of CZEs based on the standard contact algorithms enabled the modelling of such damage planes with different mesh structures (2009).

The fracture mode of the subcritical damage around the bolt holes in the CFRP specimens was not known a priori. Therefore, mixed-mode damage criteria were implemented in the present study where the subcritical damage depends on the contributions of both the Mode I and Mode II damage as illustrated in Fig. 11.

The dashed lines show the pure Mode I and Mode II traction-separation curves in their respective quadrants. The bilinear relationship for the mixed-mode subcritical damage takes its place in between those quadrants with the contributions indicated by the lower solid lines in each quadrant.
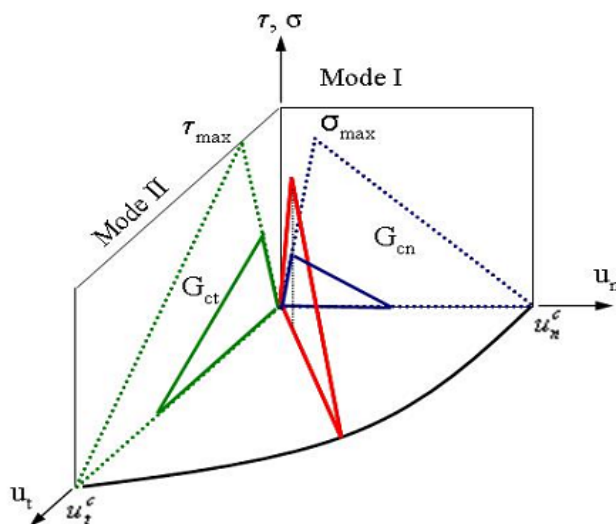

Figure 11: Bi-linear traction-separation law for mixed-mode subcritical damage.

In the mixed-mode subcritical damage, the interaction of relative contact stresses in normal and tangential directions is accounted for when calculating the initiation and growth of the damage using the following governing relations:

$$\sigma_n = \begin{cases} K_n u_n & if \quad \Delta_m \leq 1 \\ K_n u_n (1 - d_m) & if \quad \Delta_m > 1 \end{cases}$$
$$\tau_t = \begin{cases} K_t u_t & if \quad \Delta_m \leq 1 \\ K_t u_t (1 - d_m) & if \quad \Delta_m > 1 \end{cases} \tag{7}$$

where:

σ_n = normal contact stress (tension),

K_n = normal contact stiffness per unit area,

u_n = normal contact separation,

τ_t = tangential contact stress,

K_t = tangential contact stiffness per unit area,

u_t = tangential contact slip.

The parameters d_m, Δ_m and χ are defined as:

$$d_m = \left(\frac{\Delta_m - 1}{\Delta_m} \right) \chi \tag{8}$$

$$\Delta_m = \sqrt{\Delta_n^2 + \Delta_t^2}, \quad \chi = \left(\frac{u_n^c}{u_n^c - \bar{u}_n} \right) = \left(\frac{u_t^c}{u_t^c - \bar{u}_t} \right) \tag{9}$$

where: $\Delta_n = \frac{u_n}{\bar{u}_n}$

$\bar{u}_n$ = contact separation at the maximum normal contact stress,

u_n^c = contact separation at the completion of subcritical damage

$$\Delta_t = \frac{u_t}{\bar{u}_t}$$

$\bar{u}_t$ = tangential slip distance at the maximum tangential contact stress,

u_t^c = tangential slip distance at the completion of subcritical damage.

Total fracture energy at the completion of the mixed-mode damage is the sum of both the normal and tangential critical energies. A power law based energy criterion was used to define the completion of damage where the values of α and β exponents were set to 1.0:

$$\left(\frac{G_n}{G_{cn}} \right)^\alpha + \left(\frac{G_t}{G_{ct}} \right)^\beta = 1 \tag{10}$$

$$G_n = \int \sigma_n du_n \tag{11}$$

$$G_t = \int \tau_t du_t \tag{12}$$

The normal and tangential critical fracture energies are computed as:

$$G_{cn} = \frac{1}{2} \sigma_{\max} u_n^c \tag{13}$$

$$G_{ct} = \frac{1}{2} \tau_{\max} u_t^c \tag{14}$$

It was possible to confine the delamination damage planes to the areas where the delamination damage was actually observed by merging the nodes at the interfaces of the adjacent layers outside of those areas. However, such a modelling procedure

would render the general applicability of the method impractical since a peculiar interface is created whenever two different layers come into contact. Furthermore, merging between thin laminate layers is a complex operation that is prone to erroneous definitions. Therefore, a compromise between the modelling complexity and the solution time was required. Based on the experiences developed over the course of the present study, the chosen approach was to model the delamination damage planes all over the interface. As an example, the solution times for the $[90°/0°]_s$ and $[90°/0°]_{2s}$ joints are approximately 2.5 and 6 hours, respectively (Intel Core 2 Duo 3 GHz CPU, 1.95 GB of RAM).

Before attempting to predict the strength of bolted joints, it is necessary to verify the FE model predictions using experimental measurements, such as split length as a function of applied stress. However, damage in pin/bolt loaded laminates initiates at 90-95% of the ultimate load, which makes it quite difficult to measure the split/delamination growth as a function of the applied load. Figure 12 shows the development of the subcritical damage modes in pin joints of the $[90°_2/0°_2]_s$ laminates as an example (Atas 2012).
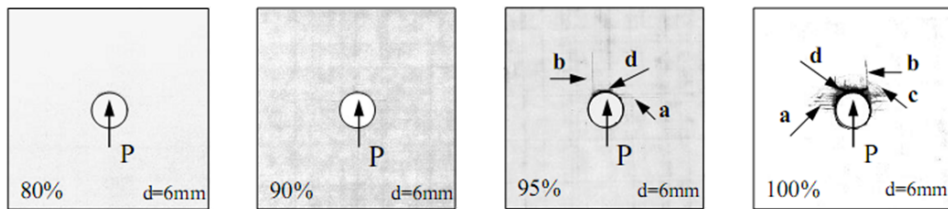

Figure 12: X-ray radiographs showing subcritical damage development in bolt joints of the $[90°_2/0°_2]_s$ laminates at 80, 90 and 95% of the average ultimate load (100%): (a) transverse matrix cracks, (b) axial splitting, (c) delamination, (d) compressive fibre failure in 0° layers (darker region).

A previous experimental study (Spearing and Beaumont 1992) showed that, in a cross-ply $[90°/0°]_s$ centre notched laminate under tensile loading, axial splitting within the 0° layers was initiated at the notch tips at relatively lower loads. They grew progressively along the fibre direction accompanied by delamination between adjacent layers. Owing to that progressive subcritical damage evolution, a cross-ply $[90°/0°]_s$ laminate with a centre notch was modelled to validate the current FE modelling approach (Atas et al. 2012, Atas et al. 2012). A good correlation was obtained between the subcritical damage predictions of the current nonlinear FE model and the experimental results (Spearing and Beaumont 1992). Together with the correlation of the contact stress distributions, this confirms that the subcritical

damage onset and growth of the bolted joints in CFRP laminates can be predicted with a reasonably good accuracy.

5   Results and discussions

Figure 13 shows the experimental and predicted load-displacement curves of the [90°/0°]$_s$ specimen as an example. The load increases in a nonlinear fashion up to point A, where the maximum load of the joint is reached. The nonlinearity is due to the nonlinear shear stress-strain response of the cross-ply laminate at early stages of the loading. The initiation and propagation of the subcritical damage modes is contributing to this nonlinearity after 90% of the maximum load. The load decreases with increased displacement after point A, since the resistance of the remaining undamaged part of the specimen ahead of the fastener reduces with increased length of the subcritical damage.

The bearing strength of the bolted joint specimens was determined by using Eq. 15, based on the maximum load carried by the joint (P_{max}) which was obtained from the numerical load-displacement curve such as that shown in Fig. 13b.

$$S_{\text{max}} = P_{\text{max}}/dt \tag{15}$$

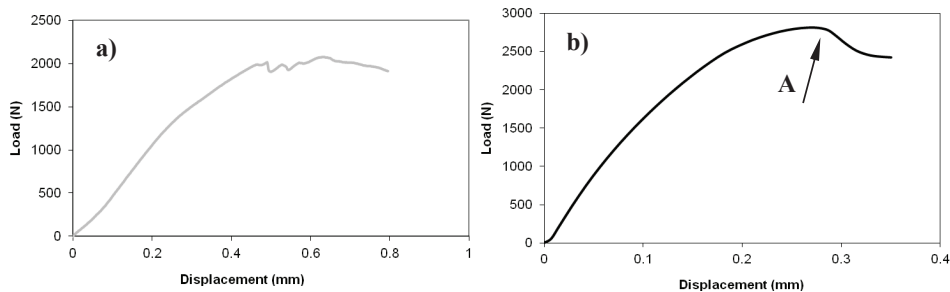where d and t are the hole diameter and specimen thickness, respectively.

Figure 13: a) Experimental and b) predicted load-displacement curve of [90°/0°]$_s$ specimen

Figures 14 and 15 show the predicted delamination damage at the 90°/0° interface and the splitting damage within the 0° layers of the [90°/0°]$_s$ specimen at the maximum load, around point A, in Fig. 13b. (Split planes within the 0° layers are shown in Fig. 8a).

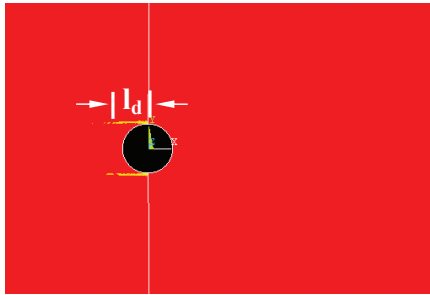Figure 14: Delamination damage at the 90°/0° interface of $[90°/0°]_s$ specimen at maximum load, P_{max}=2684.5 N (l_d: delamination length=6mm)

The approximate length of the delamination (l_d) and the splitting damages (l_s) are 6mm and 10mm, respectively, which agrees with the suggestion that the splitting drives the delamination damage (Kortschot and Beaumont 1990, Wisnom and Chang 2000). Experimental bearing strength of the joints was determined from the load-displacement curves after a significant load drop was observed according to ASTM standard (ASTM 2001), as stated earlier. Therefore, the X-ray radiographs of the failed specimens do not correspond to the maximum load carried by the joints in which the splits and other subcritical damage modes were extended up to the free edges of the specimens. This is the reason of relatively short lengths of the delamination and splits in Figs. 14 and 15, which were captured at the maximum load, but not the ultimate failure load.
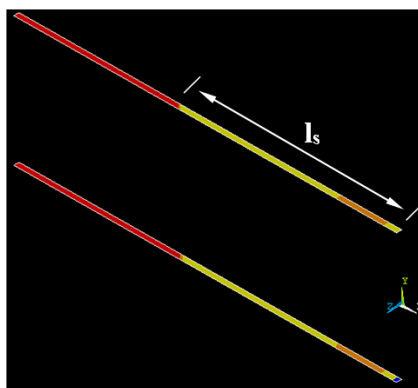

Figure 15: Splitting damage within the 0° layers of $[90°/0°]_s$ specimen at maximum load, P_{max}=2684.5 N associated with the delamination damage in Fig. 14 (l_s: split length=10mm)

In order to show the ability of the modelling approach, Fig. 16 was captured when the delamination was reached at the free edge with increased bolt displacement. The agreement of the prediction with the X-ray radiograph, Fig. 2, is good.
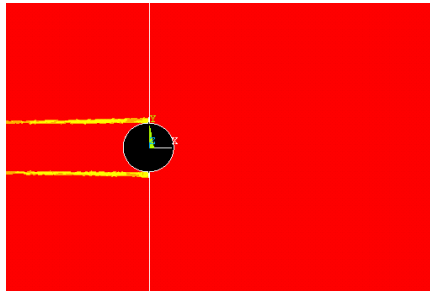

Figure 16: Delamination damage at the 90°/0° interface of [90°/0°]$_s$ specimen with increased displacement after the maximum load

Figures 17 and 18 show the predicted delamination damage at the 90°/0° interface and the splitting damage within the blocked 0° layers of the [90°$_2$/0°$_2$]$_s$ specimen at the maximum load, respectively.

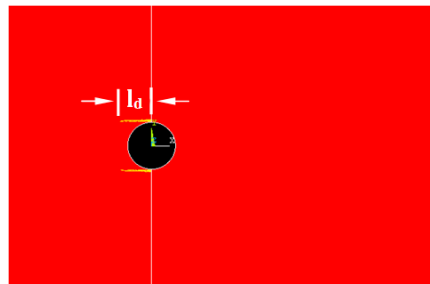Figure 17: Delamination damage at the 90°/0° interface of [90$_2$°/0$_2$°]$_s$ specimen at maximum load, P$_{max}$=4790.2 N (l$_d$: delamination length)

Figures 19 to 21 show the predicted delamination damage at the first 90°/0°, 0°/90° and the second 90°/0° interfaces of the [90°/0°]$_{2s}$ specimen at the maximum load, respectively. (The first interface is the furthest interface from the specimen mid-plane).

Figure 22 shows the splitting damage within the 0° layers of the [90°/0°]$_{2s}$ specimen. The length of the split within the first 0° layer is significantly shorter than that of the second 0° layer. (The second 0° layer is at the specimen mid-plane). This
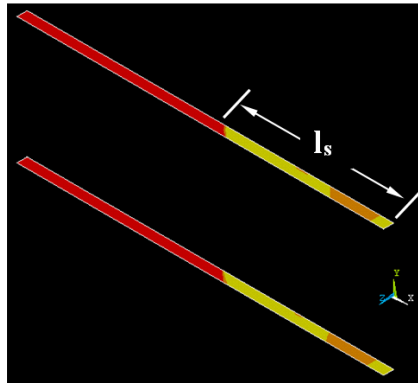
Figure 18: Splitting damage within the 0° layers of $[90_2°/0_2°]_s$ specimen at the maximum load, P_{max}=4790.2 N, associated with the delamination damage in Fig. 17 (l_s: split length)
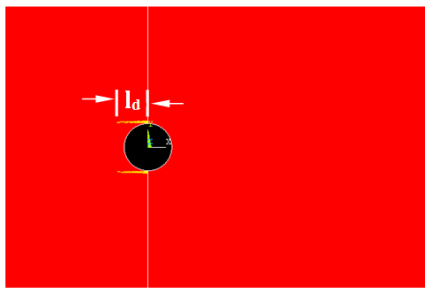

Figure 19: Delamination damage at the first 90°/0° interface of $[90°/0°]_{2s}$ specimen at maximum load, P_{max}=6145.9 N (l_d: delamination length)

difference may be explained by the number of delamination planes associated with each splitting plane as the delamination is driven by the splitting damage. The second 0° layer is connected to only one delamination plane whereas the first 0° layer is connected to two delamination planes. As a result, the splitting damage within the first 0° layer drives the delamination damage in two planes which results in a shorter splitting length.

Figure 23 compares the predicted and experimental (average of five specimens) bearing strengths of the cross-ply specimens. The maximum difference is approximately 21% for the $[90°/0°]_s$ specimen and the agreement is much improved for $[90_2°/0_2°]_s$ and $[90°/0°]_{2s}$ specimens. The small thickness of the $[90°/0°]_s$ specimens may have caused a slight bending during the experiments that could have
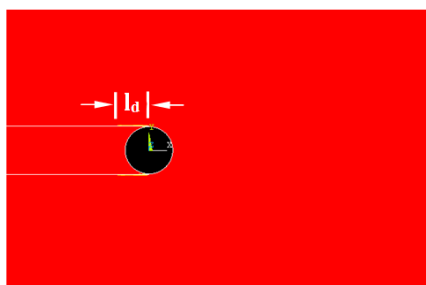
Figure 20: Delamination damage at the 0°/90° interface of $[90°/0°]_{2s}$ specimen at maximum load, P_{max}=6145.9 N (l_d: delamination length)
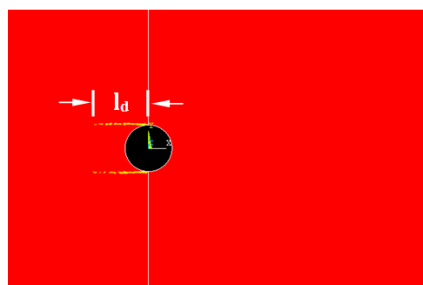

Figure 21: Delamination damage at the second 90°/0° interface of $[90°/0°]_{2s}$ specimen at maximum load, P_{max}=6145.9 N (l_d: delamination length)

contributed to the greater divergence from the predicted strength, in addition to damage introduced during the drilling of the hole and handling of the specimen during the test set up. It is suggested that the reason for the higher strength prediction of the $[90°/0°]_s$ specimen in comparison to the $[90_2°/0_2°]_s$ specimen is lower membrane stiffness (i.e. the product of the elastic modulus and thickness). Although the membrane stiffness of the $[90°/0°]_s$ specimen is the half of that $[90_2°/0_2°]_s$ specimen, both specimens have the same area of delamination planes. When the $[90°/0°]_s$ specimen is loaded, the delamination plane receives lower shear stresses with respect to the $[90_2°/0_2°]_s$ specimen since the specimen itself carries a lower load due to the lower membrane stiffness. As a result, the extent of the subcritical damage was reduced and the $[90°/0°]_s$ specimen failed at a relatively higher load level. In contrast, the extent of the subcritical damage in the $[90_2°/0_2°]_s$ specimen is higher, which results in a lower strength prediction. The same trend of the higher strength predictions with the reduced membrane stiffness was also observed for the open hole specimens in CFRP laminates under tensile loading, although this phe-
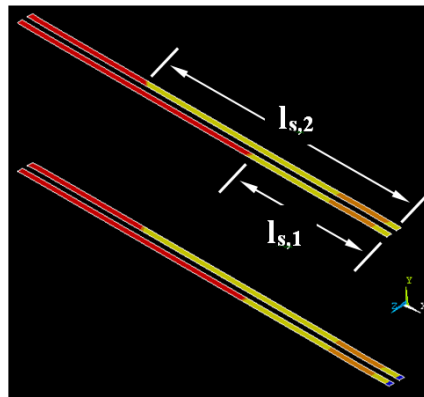
Figure 22: Splitting damage within the 0° layers of $[90°/0°]_{2s}$ specimen at maximum load, P_{max}=6145.9 N, associated with the delamination damage in Figs. 19-21 ($l_{s,1}$: split length at the first 0° layer, $l_{s,2}$: split length at the second 0° layer)
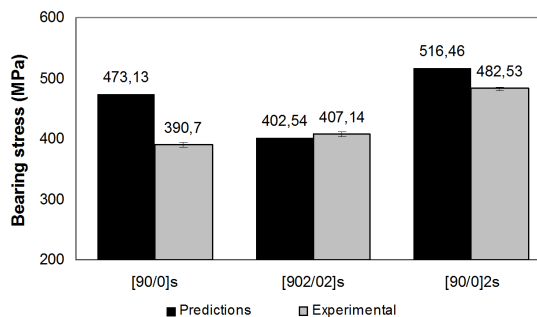
Figure 23: Predicted and experimental bearing strengths for the cross-plylay-ups (e/d=3, w/d=6)

nomenon was not associated with the membrane stiffness (Jiang et al. 2005, Hallett et al. 2009).

The increased strength of the sublaminate-level scaled $[90°/0°]_{2s}$ specimen was attributed to the interspersion of the layers, explained as follows. The global mode of failure observed in the experiments was shear-out in which the splitting within the 0° layers and the delaminations between the consecutive layers join up and shear-out the laminate ahead of the fastener (generally, as wide as the fastener diameter). Blocking the layers together (ply-level scaling), instead of interspersion, has a twofold effect on the strength of those joints. First, the splits initiate at the hole edge and grow through-the-thickness of the blocked layers without an interruption from

the adjacent layers. Second, ply-level scaling reduces the number of interfaces and therefore increases the magnitude of the shear stress to be carried by each interface (Mandell et al. 1975). As a result, greater delamination was developed under lower load levels for the ply-level scaled $[90^\circ_2/0^\circ_2]_s$ lay-up with a broader extent of transverse matrix cracking. Although this could result in stronger joints in a quasi- or near quasi-isotropic lay-up that fails in net-tension mode, by providing better stress concentration relief (Hart-Smith 1980), the larger delamination size caused global shear-out mode failure for the $[90^\circ/0^\circ]_{2s}$ cross-ply lay-up. Hence, the blocked-ply laminate configuration should be avoided due to poorer shear properties.

6   Conclusions

The success of currently used strength prediction methods for bolted joints is strongly dependant on several laminate, geometry and material system related parameters. This dependency stems from the variations in the extent of the subcritical damage modes and is generally compensated with various forms of correlation factors. The motivation of the present study was to develop a strength prediction method, based on subcritical damage modelling without resorting to experimentally determined correlation factors. Therefore, 3-D FE models were developed and the CZEs were embedded into those subcritical damage locations determined from the X-ray radiographs. CZEs use a strength-based failure criterion to predict the damage onset and a fracture mechanics based approach to predict its growth. The material properties required for simulating the subcritical damage modes were the interfacial strength, fracture energies and nonlinear matrix shear stress-strain behaviour of the particular material system used. The strength of the joints was determined from the predicted load-displacement curves. It has been shown that the effect of various laminate stacking sequences (scaling effect) on the joint strength was accounted for by the method developed.

Acknowledgements

References

ANSYS® (2009): Academic Research, Release 12.1.

ASTM (2001): D 5961/D 5961M – 01 Standard Test Method for Bearing Response of Polymer Matrix Composite Laminates. United States.

Atas, A. (2012): Strength Prediction of Mechanical Joints in Composite Laminates

Based on Subcritical Damage Modelling. PhD Thesis, The University of Sheffield.

Atas, A.; Arslan, N.; Sen, F. (2009): Failure Analysis of Laminated Composite Plates with Two Parallel Pin-loaded Holes. *Journal of Reinforced Plastics and Composites,* vol.28, no.10, pp.1265-1276.

Atas, A.; Demircioglu, T. K.; Arslan, N.; Soutis, C. (2010): Progressive Failure Analysis of Bolted Carbon Fiber/Epoxy Composite Plates. 2. National Design, Manufacturing and Analysis Congress. Balikesir,Turkey: 138-148.

Atas, A.; Mohamed, G. F.; Soutis, C. (2012): Effect of clamping force on the delamination onset and growth in bolted composite laminates. *Composite Structures*, vol.94, no.2, pp.548-552.

Atas, A.; Mohamed, G. F.; Soutis, C. (2012): Modelling delamination onset and growth in pin loaded composite laminates.*Composites Science and Technology,* vol.72, no.10, pp.1096-1101.

Atas, A.; Mohamed, G. F.; Soutis, C. (2012): Progressive failure analysis of bolted joints in composite laminates. *Plastics Rubber and Composites*, vol.41, no.4-5, pp.209-214.

Camanho, P. P.; Matthews, F. L. (1999): A progressive damage model for mechanically fastened joints in composite laminates. *Journal of Composite Materials*, vol.33, no.24, pp.2248-2280.

Chang, F. K.; Qing, X. L. (2003): Strength determination of mechanical fastened joints. Recent Advances in Structural Joints and Repairs for Composite Materials. L. Tong and C. Soutis. The Netherlands, Kluwer Academic Publishers: 101-140.

Chang, F. K.; Scott, R. A.; Springer, G. S. (1982): Strength of Mechanically Fastened Composite Joints. *Journal of Composite Materials*, vol.16, Nov, pp.470-494.

Chang, F. K.; Scott, R. A.; Springer, G. S. (1984): Failure of Composite Laminates Containing Pin Loaded Holes - Method of Solution. *Journal of Composite Materials*,vol.18, no.3, pp.255-278.

Collings, T. A.(1982): On the Bearing Strengths of Cfrp Laminates. *Composites*, vol.13, no.3, pp.241-252.

Crews, J. H.; Naik, R. A. (1986): Combined Bearing and Bypass Loading on a Graphite Epoxy Laminate. *Composite Structures,* vol.6, no.1-3, pp.21-40.

Dano, M. L.; Gendron, G.; Picard, A. (2000): Stress and failure analysis of mechanically fastened joints in composite laminates.*Composite Structures*, vol.50, no.3, pp.287-296.

Goyal, V. K.; Johnson, E. R.; Davila, C. G. (2004): Irreversible constitutive law for modeling the delamination process using interfacial surface discontinuities.

Composite Structures, vol.65, no.3-4, pp.289-305.

Hahn H. T.; Tsai, S. W. (1973):Nonlinear Elastic Behavior of Unidirectional Composite Laminae. *Journal of Composite Materials,* vol.7, pp.102-118.

Hallett, S. R.; Green, B. G.; W. G. Jiang, W. G.; Wisnom, M. R. (2009): An experimental and numerical investigation into the damage mechanisms in notched composites.*Composites Part a-Applied Science and Manufacturing*, vol.40, no.5, pp.613-624.

Harper, P. W.; Hallett, S. R. (2008): Cohesive zone length in numerical simulations of composite delamination.*Engineering Fracture Mechanics,* vol.75, no.16, pp.4774-4792.

Hart-Smith, L. J. (1980): Mechanically-Fastened Joints for Advanced Composites - Phenomenological Considerations and Simple Analyses. Fibrous Composites in Structural Design. E. M. Lenoe, D. W. Oplinger and J.J.Burke, Plenum Press, New York. 1: 543-574.

Hart-Smith, L. J. (2003): Design and analysis of bolted and riveted joints in fibrous composite structures.Recent Advances in Structural Joints and Repairs for Composite Materials. L.Tong and C.Soutis, Kluwer Academic Publishers: 211-254.

Hart-Smith, L. J. (2004): Bolted joint analyses for composite structures - Current empirical methods and future scientific prospects. *Joining and Repair of Composite Structures,* pp.127-160.

Heimbs, S.; Heller, S.; Middendorf, P.; Hahnel, F.; Weisse, J.(2009): Low velocity impact on CFRP plates with compressive preload: Test and modelling. *International Journal of Impact Engineering,* vol.36, no.10-11, pp.1182-1193.

Hollmann, K. (1996): Failure analysis of bolted composite joints exhibiting in-plane failure modes. *Journal of Composite Materials*, vol.30, no.3, pp.358-383.

Icten, B. M.; Karakuzu, R. (2002): Progressive failure analysis of pin-loaded carbon-epoxy woven composite plates. *Composites Science and Technology*, vol.62, no.9, pp.1259-1271.

Ireman, T. (1998): Three-dimensional stress analysis of bolted single-lap composite joints. *Composite Structures,* vol.43, no.3, pp.195-216.

Jiang, W. G.; Hallett, S. R.; Wisnom, M. R. (2005): Modelling of damage in composite materials using interface elements. 5th Europian LS-DYNA Users Conference, Birmingham, UK.

Jumahat, A.; Soutis, C.; Jones, F. R.; Hodzic, A. (2010): Fracture mechanisms and failure analysis of carbon fibre/toughened epoxy composites subjected to compressive loading. *Composite Structures,* vol.92, no.2, pp.295-305.

Kortschot, M. T.; Beaumont, P. W. R. (1990): Damage Mechanics of Composite-Materials .1. Measurements of Damage and Strength. *Composites Science and Technology,* vol.39, no.4, pp.289-301.

Mandell, J. F.; Wang, S. S.; Mcgarry, F. J. (1975): Extension of Crack Tip Damage Zones in Fiber Reinforced Plastic Laminates. *Journal of Composite Materials,* vol.9, Jul, pp.266-287.

McCarthy, C. T.; McCarthy, M. A.; Lawlor, V. P. (2005): Progressive damage analysis of multi-bolt composite joints with variable bolt-hole clearances. *Composites Part B-Engineering,* vol.36, no.4, pp.290-305.

McCarthy, M. A.; Lawlor, V. P.; Stanley, W. F.; McCarthy, C. T. (2002): Bolt-hole clearance effects and strength criteria in single-bolt, single-lap, composite bolted joints. *Composites Science and Technology,* vol.62, no.10-11, pp.1415-1431.

Sen, F.; Sayman, O. (2009): Experimental Failure Analysis of Two-Serial-Bolted Composite Plates. *Journal of Applied Polymer Science,* vol.113, no.1, pp.502-515.

Shokrieh, M. M.; Lessard, L. B. (1996): Effects of material nonlinearity on the three-dimensional stress state of pin-loaded composite laminates. *Journal of Composite Materials,* vol.30, pp.839-861.

Smith, P. A.; Ashby, M. F.; Pascoe, K. J. (1987): Modeling Clamp-up Effects in Composite Bolted Joints. *Journal of Composite Materials,* vol.21, no.10, pp.878-897.

Soutis, C. (1991): Measurement of the Static Compressive Strength of Carbon-Fiber Epoxy Laminates. *Composites Science and Technology,* vol.42, no.4, pp.373-392.

Soutis, C.; Fleck, N. A. (1990): Static Compression Failure of Carbon-Fiber T800/924c Composite Plate with a Single Hole. *Journal of Composite Materials,* vol.24, no.5, pp.536-558.

Soutis, C.; Fleck, N. A.; Curtis, P. T. (1991): Hole Hole Interaction in Carbon-Fiber Epoxy Laminates under Uniaxial Compression. *Composites,* vol.22, no.1, pp.31-38.

Soutis, C.; Lee, J. (2008): Scaling effects in notched carbon fibre/epoxy composites loaded in compression. *Journal of Materials Science*, vol.43, no.20, pp.6593-6598.

Spearing, S. M.; Beaumont, P. W. R. (1992): Fatigue Damage Mechanics of Composite-Materials .1. Experimental-Measurement of Damage and Post-Fatigue Properties. *Composites Science and Technology*, vol.44, no.2, pp.159-168.

Tserpes, K. I.; Papanikos, P.; Kermanidis, T. (2001): A three-dimensional pro-

gressive damage model for bolted joints in composite laminates subjected to tensile loading. *Fatigue & Fracture of Engineering Materials & Structures*, vol.24, no.10, pp.663-675.

Wang, H. S.; Hung, C. L.; Chang, F. K. (1996): Bearing failure of bolted composite joints .1. Experimental characterization. *Journal of Composite Materials*, vol.30, no.12, pp.1284-1313.

Wang, Z. Q.; Zhou, S.; Zhang, J. F.; Wu, X. D.; Zhou, L. M. (2012): Progressive failure analysis of bolted single-lap composite joint based on extended finite element method. *Materials & Design*, vol.37, pp.582-588.

Waszczak, J. P.; Cruse, T.(1971): Failure Mode and Strength Predictions of Anisotropic Bolt Bearing Specimens.*Journal of Composite Materials*, vol.5, pp.421.

Whitney, J. M.; Nuismer, R. J. (1974): Stress Fracture Criteria for Laminated Composites Containing Stress-Concentrations. *Journal of Composite Materials*, vol.8, Jul, pp.253-265.

Whitworth, H. A.; Aluko, O.; Tomlinson, N. A. (2008): Application of the point stress criterion to the failure of composite pinned joints. *Engineering Fracture Mechanics*, vol.75, no.7, pp.1829-1839.

Wisnom, M. R.; Chang, F. K. (2000): Modelling of splitting and delamination in notched cross-ply laminates. *Composites Science and Technology*, vol.60, no.15, pp.2849-2856.

Xiao, Y.; Ishikawa, T. (2005): Bearing strength and failure behavior of bolted composite joints (part II: modeling and, simulation). *Composites Science and Technology*, vol.65, no.7-8, pp.1032-1043.